Computational Particle Mechanics (2024) 11:1007–1020
https://doi.org/10.1007/s40571-023-00669-9

Microscopic mechanical analysis of K_0 of granular soils with particle size distribution and rolling resistance effects

Tao Zhang[1,2,3] · Sui Wang[1] · Shuyang Yu[1] · Zhaohua Sun[1] · Chuanfeng Fang[4] · Shuren Wang[2]

Received: 16 July 2023 / Revised: 12 September 2023 / Accepted: 22 September 2023 / Published online: 25 October 2023

Abstract

The coefficient of lateral earth pressure at rest, K_0, is an essential parameter for analyzing earth pressure distribution and the safe reliability of structures in geotechnical engineering. This paper presents a series of numerical one-dimensional compression tests on granular soils with particle size distribution (PSD) and rolling resistance (RR) effects using a real-particle 3D discrete element model. The corresponding macro–micro behaviors are investigated in a parallel way. Both PSD and RR affect K_0 and the related compression characteristics. A higher coefficient of uniformity (C_u) or rolling resistance coefficient (μ_r) results in a monotonic decrease in the mean coordination number, and too much consideration of RR makes the mean coordination number less realistic in a particle system. The influence of PSD is more sensitive to the local-ordering structure and contact force network than the RR. The inhomogeneity of normal contact forces enhances as C_u increases and slightly reduces as μ_r increases. The strong contacts are much more anisotropic than the weak ones. Specimen with lower C_u or higher μ_r induces higher anisotropy and more strong contacts during compression, in which a lower K_0 is measured. A unique macro–micro relationship exists between K_0 and deviatoric fabric when strong contacts are considered only.

Keywords Coefficient of lateral earth pressure · Discrete element method · Particle size distribution · Rolling resistance · Fabric anisotropy

1 Introduction

The coefficient of lateral earth pressure at rest, K_0, is commonly used to quantify the effective horizontal earth pressure, which is relevant to many geotechnical engineering issues, including tunnels, pile foundations, high rockfill dams, and deep shaft walls [1–3]. K_0 represents the ratio between the effective horizontal pressure (σ'_h) and the effective vertical pressure (σ'_v) under the condition of zero horizontal movements. Although the mathematical description is given clearly, there is no fully accepted theoretical calculation of K_0 [2, 4, 5]. In practice, the widely-used K_0 equation proposed by Jaky [6] is adopted to predict the values of K_0, which is simply related to the internal friction angle of granular soils and given as follows

$$K_0 = 1 - \sin \phi' \tag{1}$$

✉ Shuren Wang
shurenwang@hpu.edu.cn

Tao Zhang
zhangtao080818@163.com

Sui Wang
wangsui_9135@163.com

Shuyang Yu
yushuyang_hhu@163.com

Zhaohua Sun
sunzhaohua@ntu.edu.cn

Chuanfeng Fang
1010121@hnust.edu.cn

1 School of Transportation and Civil Engineering, Nantong University, Nantong 226000, China

2 International Joint Research Laboratory of Henan Province for Underground Space Development and Disaster Prevention, Henan Polytechnic University, Jiaozuo 454003, China

3 State Key Laboratory for Geomechanics and Deep Underground Engineering, China University of Mining and Technology, Xuzhou 221116, China

4 School of Resources, Environment and Safety Engineering, Hunan University of Science and Technology, Xiangtan 411201, China

where ϕ' stands for the internal friction angle of granular soils. Numerous researchers have verified the validity of Eq. (1) through experimental studies [1, 2, 7–9].

On the whole, most previous experimental methods on the measurement of the stress states of granular soils under at-rest or K_0 conditions fall into four classes: flexible or thin wall oedometer tests [1, 4, 8, 10, 11], rigid wall oedometer tests [5, 12–15], triaxial compression tests [16–19], and in-situ shear wave velocity tests [20–23]. The K_0 condition means zero horizontal strain and movement. Talesnick [5] stressed that the testing methodology must have the capacity to properly maintain at-rest soil conditions and accurately measure soil pressures. However, the flexible or thin wall oedometers and the triaxial cells can hardly control the specimen to be zero horizontal strain as axial strain increases, making the mechanical state inconsistent with the K_0 condition. Unlike the triaxial cells, the main drawback of the rigid wall oedometers is the existence of frictional stress generating on the soil-wall interface, which reduces the vertical pressure and makes the vertical pressure imprecise along the height, especially for the soils under high-pressure loading. The seismic wave method is susceptible to environmental disturbance and is limited to surveying depth.

It is fortunate that the discrete element method (DEM) proposed by Cundall and Strack [24] enables overcoming the limitations in experimental tests and allows a link between macro and micro mechanical behaviors. With DEM, numerous studies have been carried out to investigate the macroscopic factors affecting the microstructure of granular soils and how the microstructure further affects K_0. For example, Gu et al. [25, 26] found that K_0 of a certain soil depends on the coordination number regardless of the void ratio. Lopera Perez et al. [27] reported that K_0 increases with void ratio, and the variation of K_0 is related to the degree of structural anisotropy and normal contact force anisotropy. Khalili et al. [28] prepared both isotropic and anisotropic samples in the initial state and found that K_0 is related to the evolution of force anisotropy. Chen et al. [29] conducted a series of DEM simulations with two kinds of particle shapes and built a relationship between K_0 and anisotropy of fabric measures (i.e., contact normal and contact force).

These published results have clearly shown that K_0 is related to many factors, including void ratio [8, 16, 18, 25, 27], friction angle [1, 2, 5, 6], initial preparation method [13, 15, 26, 28, 30], stress history [1, 2, 5, 7, 13], particle shape [8, 29, 31, 32], and particle size distribution (PSD) [15]. Of these, it is well recognized that particle shape and PSD significantly influence the mechanical responses of granular soils. For example, Zhu et al. [15] found that K_0 of gravel decreases with increasing maximum particle size under the same effective vertical stress. Still, studies of the effect of PSD on K_0 for traditional sands are reported rarely. Guo and Stolle [33] found that the relation between K_0 and particle shape is not unique because the variation of particle shape may change particle connectivity. Lee et al. [8] showed that the correlation of K_0 to ϕ' is effective for uniformly round particles, while some errors exist in angular ones due to interlocking effects. Based on the mobilized strength and inter-particle resistance between particles, Lee et al. [8] further proposed an inter-particle strength-based relationship for describing K_0, which takes the interlocking effect into account. Nevertheless, the effect of particle shape on K_0 remains unclear due to the differences in testing methods and diversities in particle shapes. Particle shape quantification based on shape parameters, such as sphericity, aspect ratio, convexity, roundness, roughness, and overall regularity [34–46], is not only complicated but also difficult to evaluate the microstructure at the particle level. To take the effect of particle shape into account for simplicity, a common method is to incorporate a torque acting on each particle to counteract the rolling motion, i.e., rolling resistance (RR) [47–52]. However, the effect of RR on K_0 of granular soils has not been thoroughly analyzed.

The paper aims to examine the effects of PSD and RR on K_0 of granular soils using 3D DEM with non-spherical particles. The non-spherical particles enable a more realistic simulation and a better understanding of the macro- and micro-mechanical responses of granular soils during K_0 conditions. Numerical results are analyzed in detail from macroscopic and microscopic points of view, e.g., evolutions of K_0, coordination number, contact force distribution, and fabric anisotropy.

2 DEM model description

A series of one-dimensional compression tests were numerically conducted using 3D DEM to study the effects of PSD and RR on K_0 of granular soils. The RR model employed here is based on the linear model, to which a RR mechanism is added [53–57], as shown in Fig. 1. The interaction response between particles includes the normal, tangential, and rotational forces. The contact forces satisfy the following equations:

$$\begin{cases} \left|\boldsymbol{f}_n\right| = k_n|\boldsymbol{\delta}| \\ \left|\boldsymbol{f}_s\right| = \min\left\{\left|\boldsymbol{f}'_s + k_s\Delta\boldsymbol{u}\right|,\ \mu\left|\boldsymbol{f}_n\right|\right\} \end{cases} \tag{2}$$

where k_n and k_s are the normal and shear stiffness constants, $\boldsymbol{\delta}$ is the penetration depth of two particles at contact, $\Delta\boldsymbol{u}$ is the relative displacement at each time step, $\boldsymbol{f}_n$ and $\boldsymbol{f}_s$ are the normal and shear contact forces, $\boldsymbol{f}'_s$ is the previous shear contact force, and μ is the interparticle friction coefficient. Given a particle, its motion satisfies the following Newton–Euler equations:

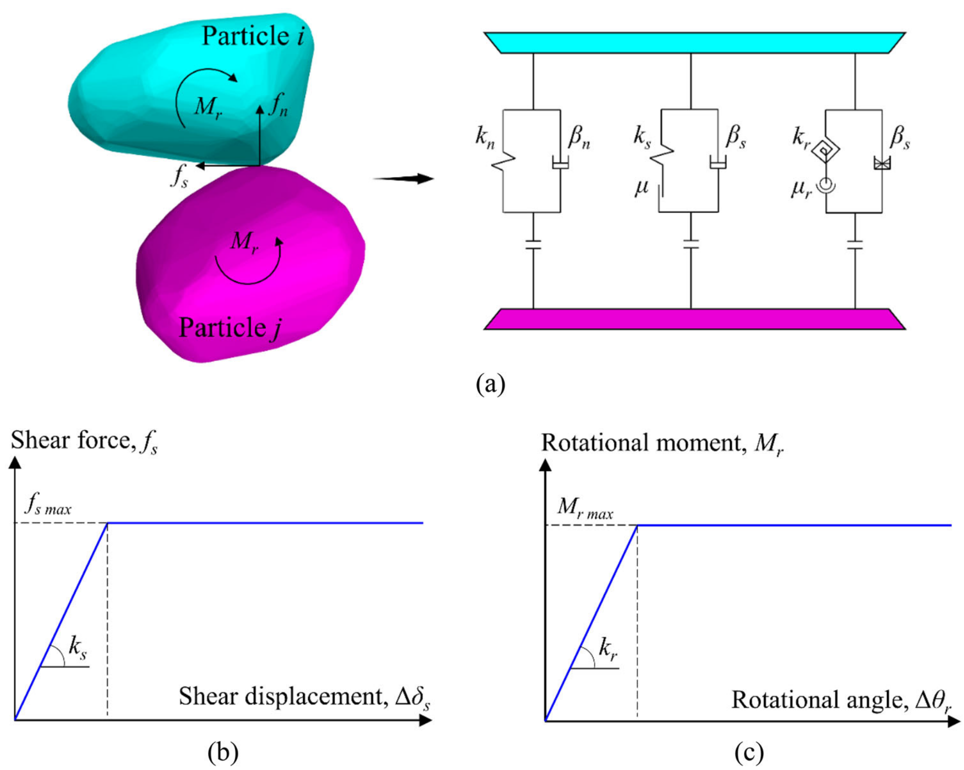

Fig. 1 The rolling resistance linear model in DEM: **a** behavior and rheological components of the model; **b** shear force–displacement law; **c** rotational moment–angle law

$$m_i \frac{dv_i}{dt} = \sum_{c=1}^{n_c} \left(f_i^l + f_i^d \right) + m_i g \tag{3}$$

$$I_i \frac{d\omega_i}{dt} - \left(I_j - I_k \right) \omega_j \omega_k = \sum_{c=1}^{n_c} \left(M_i^s + M_i^r \right) \tag{4}$$

where i, j, k are subsequent indexes, m_i is the particle mass, v_i is the translational velocity, n_c is the number of contacts, ${f_i}^l$ is the elastic force at contact c, ${f_i}^d$ is the viscous damping force at contact c, ω_i is the angular velocity, I_i is the principal moment of inertia, and ${M_i}^s$ and ${M_i}^r$ are the moments caused by the shear force and RR at contact c. The RR moment M^r is given by

$$M^r = \begin{cases} M^r, \ \| M^r \| \leq \mu_r \overline{R} f_n \\ \mu_r \overline{R} f_n, \ \text{otherwise} \end{cases} \tag{5}$$

$$M^{r*} = M^r - k_r \Delta\theta_r \tag{6}$$

where μ_r is the RR coefficient, k_r is the RR stiffness, $\Delta\theta_r$ is the incremental rotational angle in the rolling direction, and $\overline{R}$ is the effective contact radius. The normal stiffness k_n is given by

$$k_n = \frac{\pi r^2 E^*}{r_1 + r_2} \tag{7}$$

Table 1 Parameters used in the DEM

Particle density ρ (kg/m^3)	2650
Normal stiffness of ball k_n (N/m)	3×10^6
Shear stiffness of ball k_s (N/m)	3×10^6
Normal and shear stiffness of wall (N/m)	3×10^8
Damp ratio	0.2
Friction coefficient between wall and ball	0.0

where E^* is the effective modulus, r_1 and r_2 are the equivalent radii of particles 1 and 2, and r equals min (r_1, r_2). The shear stiffness k_s is calculated via $k_s = k_n/\kappa^*$, where κ^* is the normal-to-shear stiffness ratio. The RR stiffness k_r is calculated via $k_r = k_s \overline{R}^2$.

The specimen used in the 3D DEM was represented in a cylinder (Φ 10 mm × 20 mm) by several strain or stress-controlled rigid and frictionless walls. The specimen is kept small to improve computing efficiency and has sufficient size to capture the mechanical behavior while reducing the size effect as the specimen diameter is larger than 8 × mean particle size d_{50} [57]. The input parameters for DEM simulations are listed in Table 1. Figure 2a shows the PSDs of sands modeled in this study. The properties of the PSDs can be characterized by different parameters, such as coefficient of uniformity (C_u), and mean particle size (d_{50}). In this study, d_{50} is fixed as 1.2 mm for all specimens, and C_u varies from 1.0 to 2.7. The non-spherical particle used in the model is

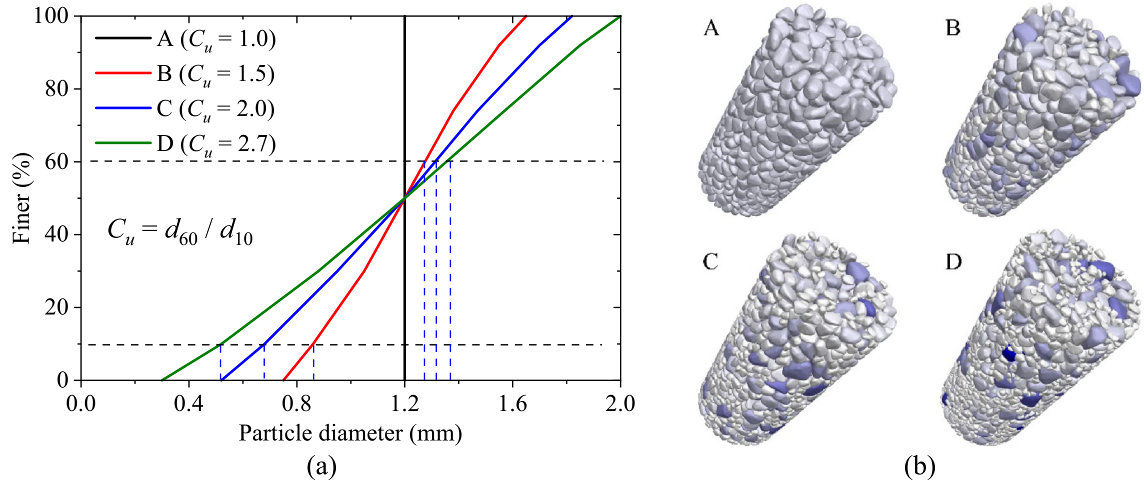

Fig. 2 **a** Particle size distributions and **b** specimens with non-spherical particles modeled in the DEM simulations

Table 2 Details of the tested specimens

PSD type	C_u	d_{50}/mm	μ	μ_r
A	1	1.2	0.5	0.1
B	1.5	1.2	0.5	0.1
C	2.0	1.2	0.5	0.1
D	2.7	1.2	0.5	0.0
				0.1
				0.2
				0.4

convex, as shown in Fig. 2b, and its corresponding sphericity and aspect ratio are 0.864 and 0.738, respectively. Sphericity [58] is defined as the surface ratio of a sphere having the same volume as the particle to the surface of the particle itself, i.e. $S = \sqrt[3]{36\pi V^2} \Big/ \mathrm{SA}$, where V = the volume of a particle, and SA = the surface area of a particle. Aspect ratio describing the anisotropy of the form of a particle is the mean of the elongation index (EI = b/a) and flatness index (FI = c/b) (i.e., a, b, and c refer to the major, intermediate, and minor principal dimensions respectively). Table 2 lists the simulation plan in this study.

The specimen was randomly distributed and then rearranged without overlap between particles in the cylinder wall. The interparticle friction coefficient μ was temporarily set to zero during this rearrangement. The initial void ratio of all specimens was 0.562, and the corresponding particle numbers were 1111, 1400, 2108, and 4076, respectively. Then the specimens were compressed in the one-dimensional condition by moving the top and bottom walls towards each other with the constant rate of 0.01 m/s until the vertical stress σ_v reached 10 MPa. The one-dimensional compression process is performed with the constant interparticle friction coefficient ($\mu = 0.5$) and different RR coefficients varying from 0.0 to 0.4.

3 Results and discussion

3.1 Typical macroscale behaviors

In Fig. 3, the one-dimensional compression responses of specimens with different PSDs are presented. A-0.1 means that a specimen of grading A was compressed with an μ_r of 0.1. The K_0 values of the specimen with a larger C_u run above those with lower C_u, as shown in Fig. 3a. The lower values of K_0 from the specimen with a lower C_u can be attributed to the strong force chain along the vertical direction due to more significant interlocking, simultaneously resulting in a lower degree of stress transfer in the horizontal direction. From the e-lgσ_v curves shown in Fig. 3b, it is also observed that the specimen with lower C_u is harder to compress, further indicating that more strong forces are along the vertical direction and form a more solid skeleton.

Figure 4 shows the one-dimensional compression responses of specimens with different RR coefficients. The K_0 values of the specimen with a lower μ_r run above those with a higher μ_r, as shown in Fig. 4a. Similar to the above, the lower values of K_0 from the specimen with a higher μ_r can be attributed to the strong force chain along the vertical direction due to more intense friction between particles, resulting in a lower degree of stress transfer in the horizontal

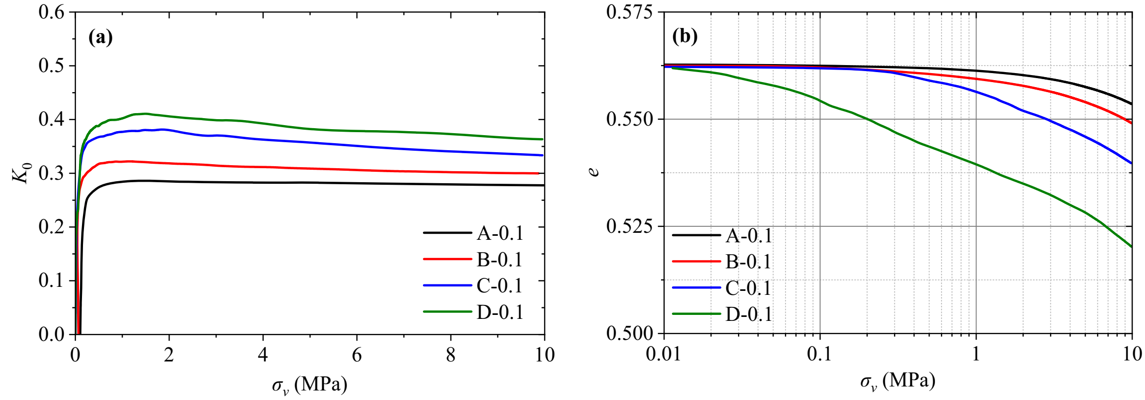

Fig. 3 Particle size distribution effect on the macroscale behaviors: **a** K_0; **b** e

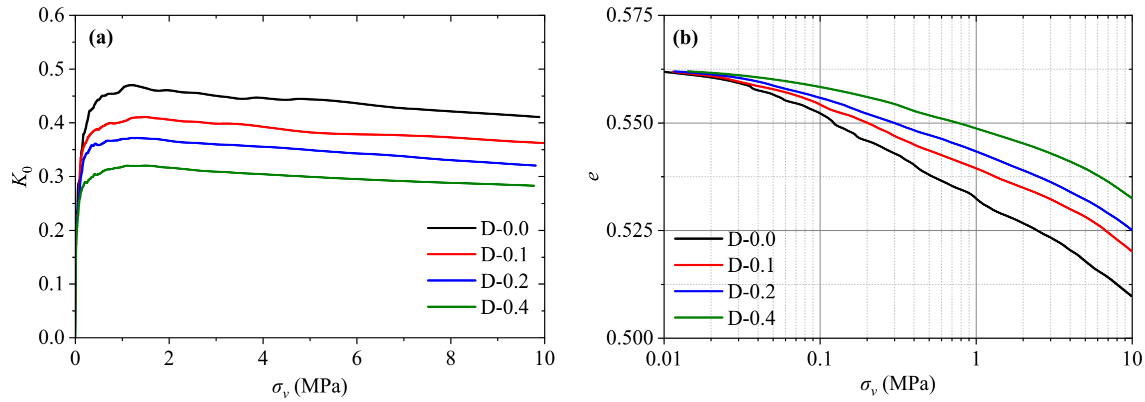

Fig. 4 Rolling resistance effect on the macroscale behaviors: **a** K_0; **b** e

direction. Figure 4b reveals that the specimen with a higher μ_r forms a more solid skeleton. The effect of RR on the K_0 values can be identified by comparing the results from Lee et al. [8], who found that the K_0 values for irregular sands are lower than those for glass beads due to the higher degree of friction and interlocking between particles.

3.2 Coordination number

One advantage of DEM modeling is that the evolution of microscale response can be observed and analyzed to reveal the underlying mechanism. The coordination number (CN) quantifies the contact number of each particle and reflects the microstructural evolution. The mean CN defined by Thornton and Antony [59] is given by

$$Z = \frac{2N_c - N_p^1}{N_p - N_p^0 - N_p^1} \tag{8}$$

where N_c = the total contact number, N_p = the total particle number, N_p^0 and N_p^1 = numbers of particles with zero and one contact, respectively. The reason for this definition is that particles with no contact or one contact miss the contribution to stress transmission.

Figure 5a shows the evolutions of mean CNs under the PSD effect. It can be seen that Z increases rapidly with increasing vertical stress at the early stage and then gradually stabilizes. The higher C_u, the lower Z is. It means that a wide particle grading range increases the number of floating particles with contact numbers less than two, as shown in Figs. 6 and 7. Figure 6 also shows the evolution of the percentage of particles with more than one contact N_p^2; it is observed that the percentage of N_p^2 decreases with increasing C_u. The mean CNs for A-0.1, B-0.1, C-0.1, and D-0.1 at 10 MPa are nearly 6.89, 6.01, 5.62, and 4.84, respectively, and the relative mean CNs (R_{CN}, ratios of A-0.1, B-0.1, C-0.1, and D-0.1 to A-0.1) are 1.000, 0.872, 0.816, and 0.702, which decrease with increasing relative C_u (R_{Cu}). Figure 8 shows the relationship between R_{CN} and R_{Cu} as the vertical stress ranges from 0.5 to 10 MPa, and the result indicates that R_{CN} decreases linearly with increasing R_{Cu} regardless of the influence of vertical stress.

Figure 5b shows the evolutions of CNs under the RR effect. It can be seen that increasing μ_r causes a monotonic decrease in the mean CN, where specimen D-0.4 has the

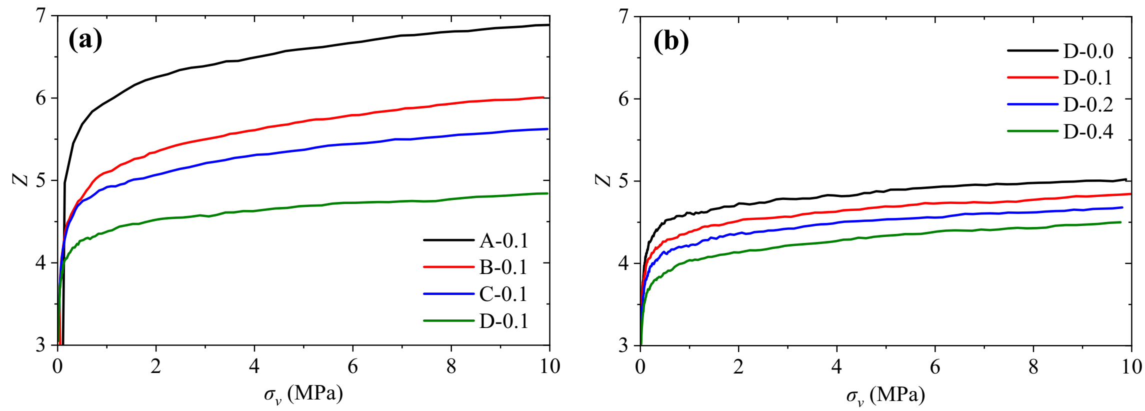

Fig. 5 Evolutions of coordination number during one-dimensional compressions: **a** PSD effect; **b** RR effect

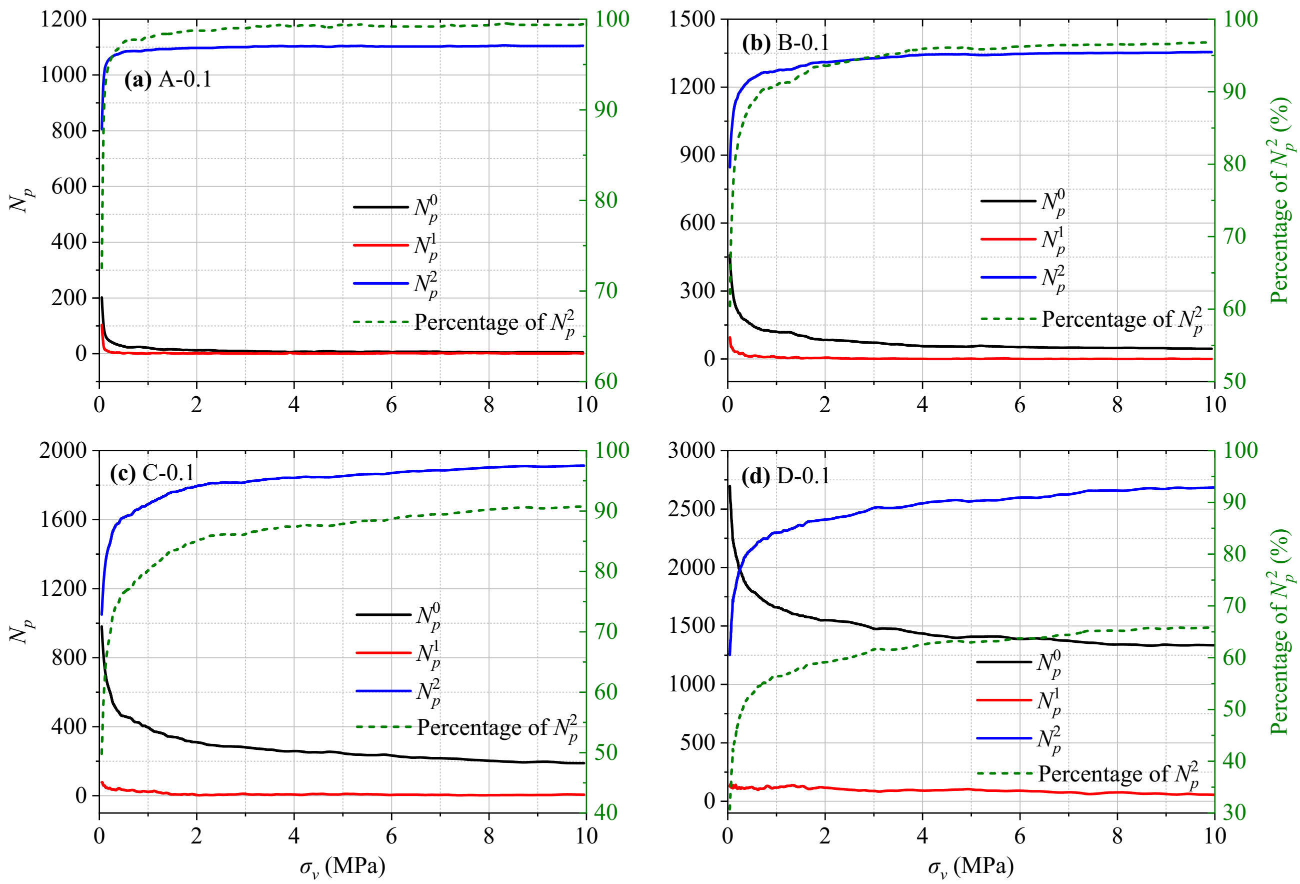

Fig. 6 Evolutions of particle numbers for particles with no contact, one contact, and more than one contact: **a** A-0.1; **b** B-0.1; **c** C-0.1; **d** D-0.1

lowest mean CN (3.5–4.5) throughout the simulation. Previous simulation studies of frictional spheres compressed in a gravity-free environment have shown that the mean CN is significantly larger than 4.5 [60]. Existed CT scanning tests of silica sands have reported that the mean CN is larger than 6 as the vertical stress reaches 10 MPa [38, 61]. Obviously, too much consideration of RR makes the mean CN less realistic in a particle system [52].

3.3 Radial distribution function

The radial distribution function (RDF), used to explore the local-ordering structure of a granular assembly, is the probability of finding the center of a particle within a spherical shell at a certain distance from a reference particle [62]. The RDF is defined as follows:

Fig. 7 Illustrations of particles with no contact (burgundy), one contact (bright blue), and more than one contact (gray)

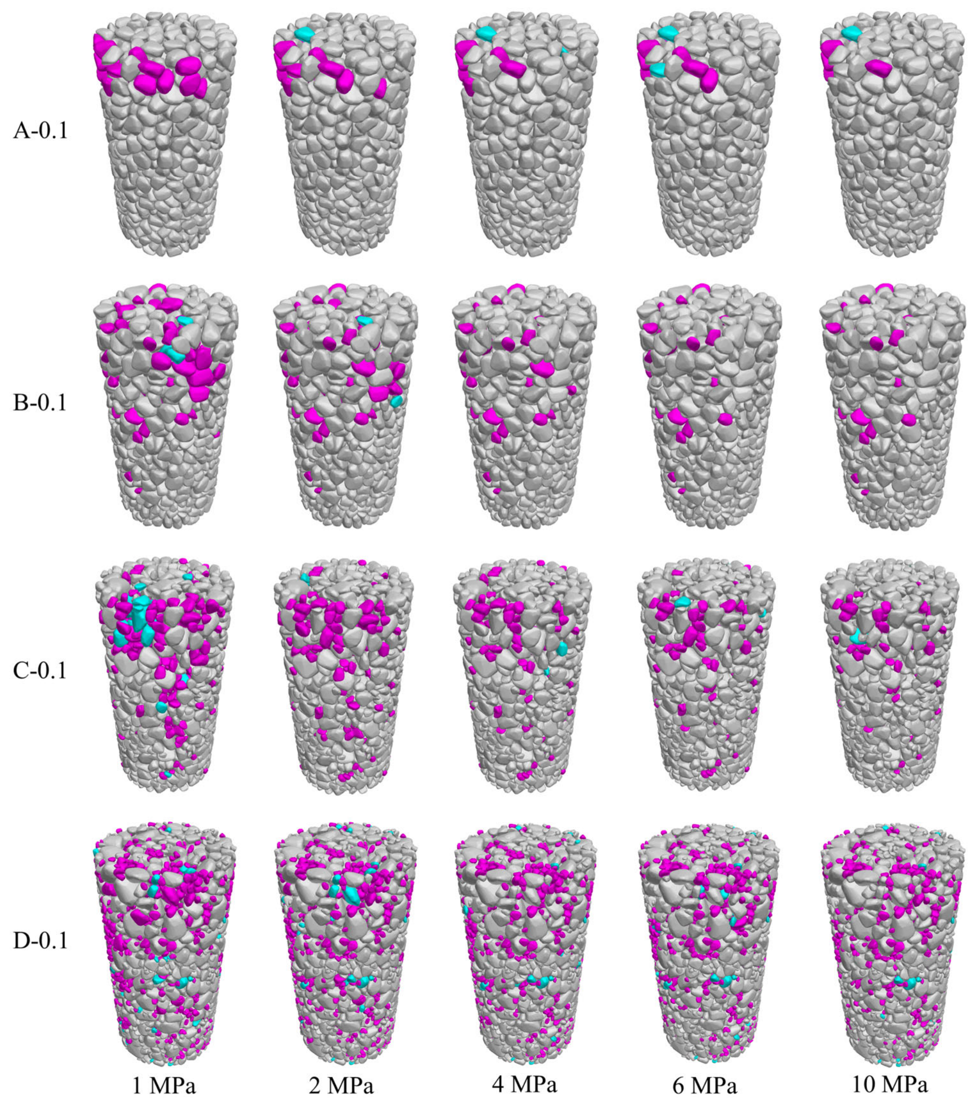

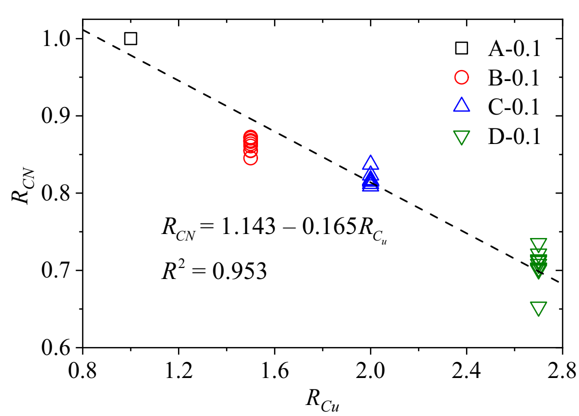

Fig. 8 Relationship between R_{CN} and R_{Cu} in a wider range of vertical stress

$$n(r_2) - n(r_1) = \int_{r_1}^{r_2} g(r) 4\pi r^2 dr \tag{9}$$

where $n(r)$ is the number of particles within a spherical shell of radius r. Figure 9 shows the normalized radial distribution of particle numbers in a spherical shell as a function of the dimensionless distance $r/\langle d\rangle$, where $\langle d\rangle$ is the mean particle diameter. For the monodisperse particles in Fig. 9a, a clear first peak of $g(r)$ can be seen at $r/\langle d\rangle$ less than 1. This position of the first peak is consistent with the result from Conzelmann et al. [63] and is lower than the position for spherical particles ($r/\langle d\rangle = 1$) [62, 64, 65]. Then, $g(r)$ decreases to minimum at $r = 1.6\ \langle d\rangle$ indicating a minimum probability of finding particles in contact. $g(r)$ continues to increase to another peak at $r = 2.35\ \langle d\rangle$. RDF of the specimen with higher C_u shows different behaviors; the first peak ($r/\langle d\rangle < 1$) shifts to a lower value, and the peak is more prominent, representing the higher coordination of the polydisperse specimen compared with the monodisperse one and also indicating an increasing organization in the packing structure [65–67].

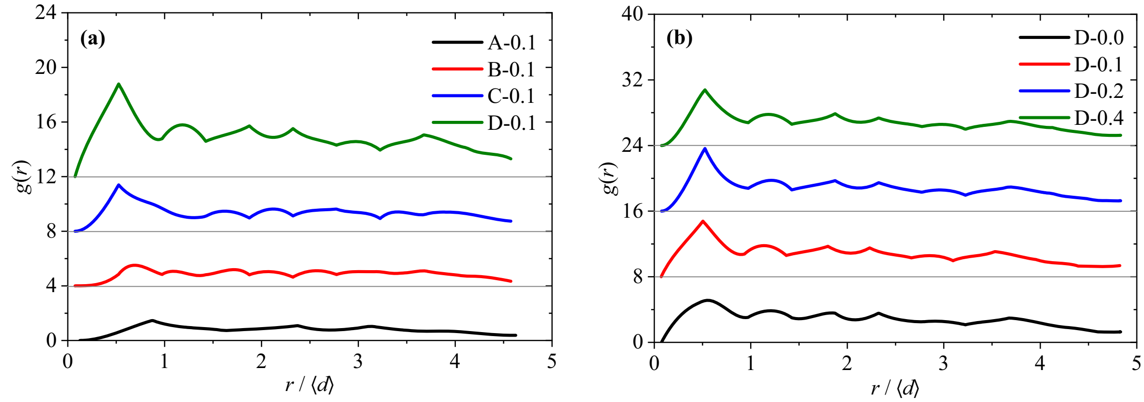

Fig. 9 Radial distribution functions for specimens with **a** different PSDs and **b** different RR coefficients

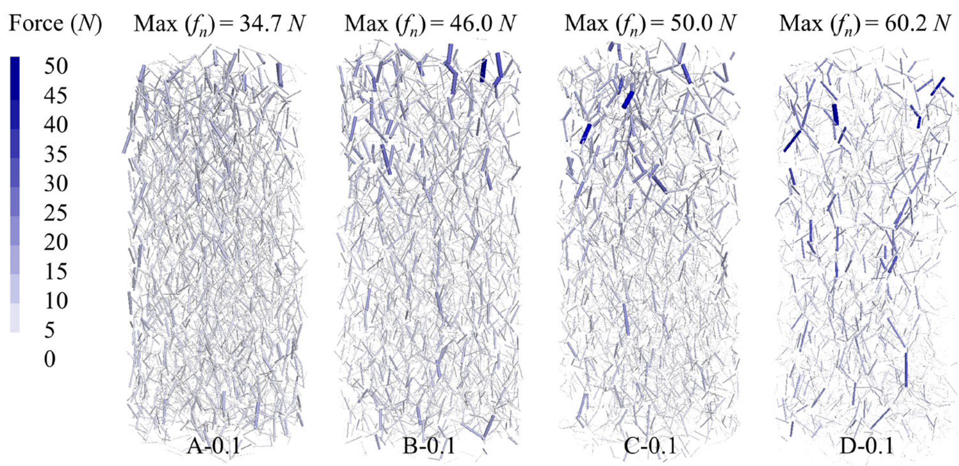

Fig. 10 Closeup views of the contact force network under the vertical stress of 10 MPa

Figure 9b shows the RDFs of the four specimens with different RR coefficients. The first peak of an RDF appears at the same position $r = 0.5 \langle d \rangle$, regardless of RR. Additionally, the number of peaks and the corresponding amplitudes is almost identical regardless of RR. Similar results have been found by Zhao et al. [67] that the position of the first peak is independent of particle shape, and Kramar et al. [68] found that the RDF is regardless of the friction coefficient.

3.4 Contact force

The microstructure of granular materials can be described in terms of force chain characteristics. Figure 10 presents the closeup views of the contact force network in A-0.1, B-0.1, C-0.1, and D-0.1 as the vertical stress equals 10 MPa. As C_u increases, the distribution of forces broadens, which reflects in the increase in the maximum contact force.

The probability distribution function (PDF) of the contact force is commonly used to quantify the contact force network. For the specimen with monodisperse particles ($C_u = 1$), the PDF for normal contact force f_n less than the average $\langle f_n \rangle$ fits well with the Gaussian distribution (see Fig. 11a) defined as

$$\mathrm{PDF}(f_n) = a + \frac{b}{c\sqrt{\pi/2}} e^{-2(f_n/\langle f_n \rangle - d)^2/c^2} \tag{10}$$

where a, b, c, and d are fitting parameters of the Gaussian function. As C_u increases, PDF(f_n) has an upturn at very small forces and PDF(f_n) fits well with the power law (see Fig. 11b–d)

$$\mathrm{PDF}(f_n) = \beta_2 \left(f_n / \langle f_n \rangle \right)^{\beta_1} \tag{11}$$

where β_1 and β_2 are fitting parameters of the power function. As usually observed, PDF(f_n) above $\langle f_n \rangle$ for each specimen is characterized by an exponential distribution

$$\mathrm{PDF}(f_n) = \alpha_2 e^{-\alpha_1 (f_n/\langle f_n \rangle)} \tag{12}$$

where α_1 and α_2 are fitting parameters of the exponential function. Notably, the differences in the PDF(f_n) for a certain specimen are almost negligible. That is, PDF(f_n) maintains a nearly constant distribution regardless of the influence of

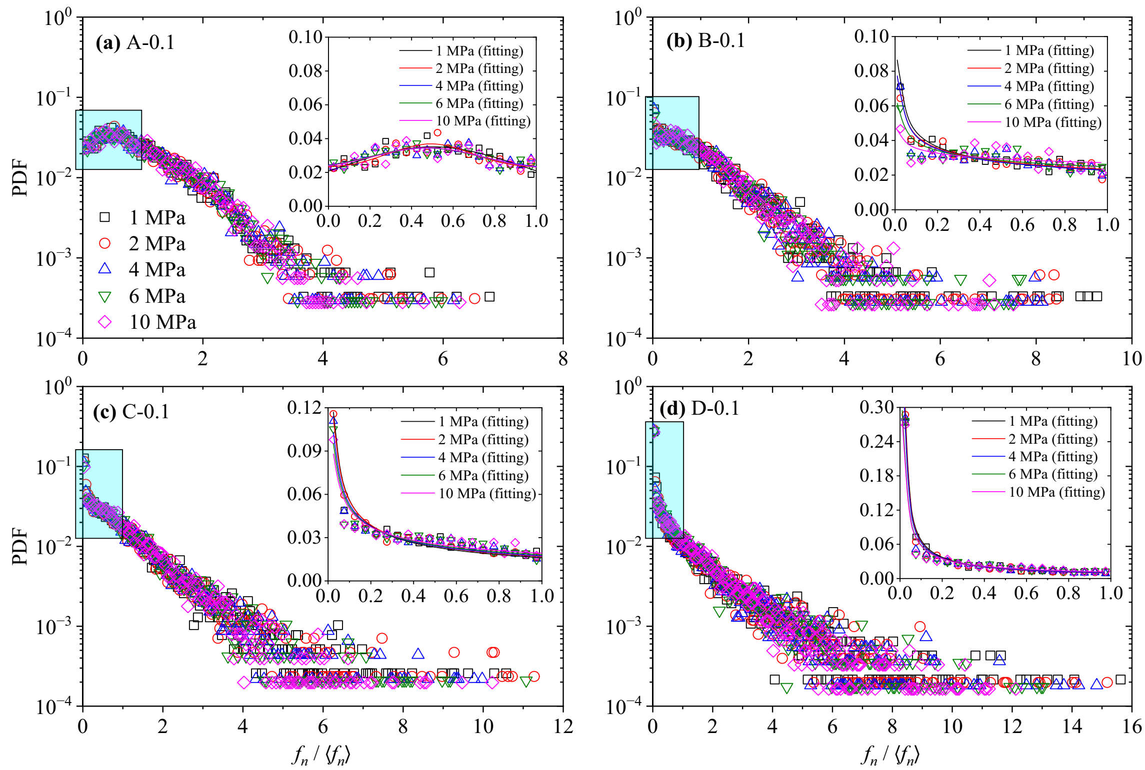

Fig. 11 Probability distribution function of normal contact forces f_n normalized by the average $\langle f_n \rangle$ in log-linear scale: **a** A-0.1; **b** B-0.1; **c** C-0.1; **d** D-0.1

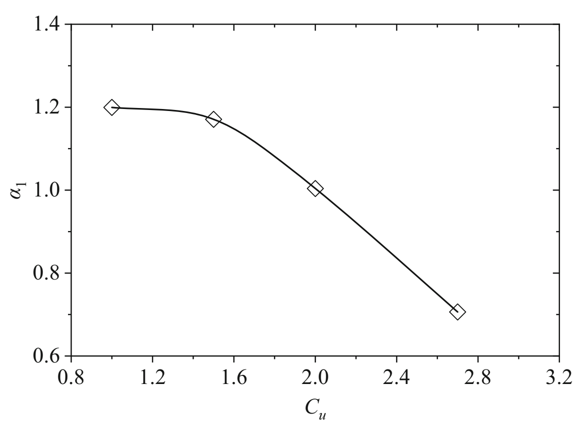

Fig. 12 Variation trend of α_1

vertical stress. The main reason for this phenomenon is that the stress field or K_0 in a one-dimensional state is less varied. The result is in accordance with the findings in previous one-dimensional tests [37], and isotropic compression tests [69, 70]. Additionally, Fig. 11 shows that the distribution of normal forces varies in the other two ways as C_u increases. One is that the distribution becomes broader with the average of α_1 decreasing from 1.20 to 0.71, as shown in Fig. 12, and maximum forces get to be as large as sixteen times the average, implying that the inhomogeneity of normal forces enhances as C_u increases. Another is that the average proportion of weak contacts increases from 59.29% for $C_u = 1$ to 68.77% for $C_u = 2.7$. Similar observations were made in 2D DEM simulation investigated by Estrada and Oquendo [71], and 3D simulations investigated by An et al. [72], Cantor et al. [73], and Mutabaruka et al. [74].

Figure 13 shows the PDF(f_n) of normal forces normalized by the average under the effect of RR. It can be seen that the PDF(f_n) below $\langle f_n \rangle$ for each specimen fits well with the power law, and the PDF(f_n) above $\langle f_n \rangle$ is characterized by an exponential distribution, implying that the function type of PDF(f_n) is independent of RR. The average proportion of weak contacts decreases slightly from 69.36% for $\mu_r = 0.0$ to 67.96% for $\mu_r = 0.4$. The average of α_1 increases from 0.66 for $\mu_r = 0.0$ to 0.77 for $\mu_r = 0.4$ in a narrow range, indicating that the homogeneity of normal forces slightly enhances as μ_r increases.

The second-order fabric tensor introduced by Satake [75] is frequently used to quantify the fabric anisotropy, which characterizes the distribution in contact normal orientations.

$$\phi_{ij} = \frac{1}{N_c} \sum_{k=1}^{N_c} n_i^k n_j^k (i,\ j = x,\ y,\ z) \tag{13}$$

where n_i^k = the contact normal vector of the contact k in the ith direction. The principal values of ϕ_{ij}, ordered by

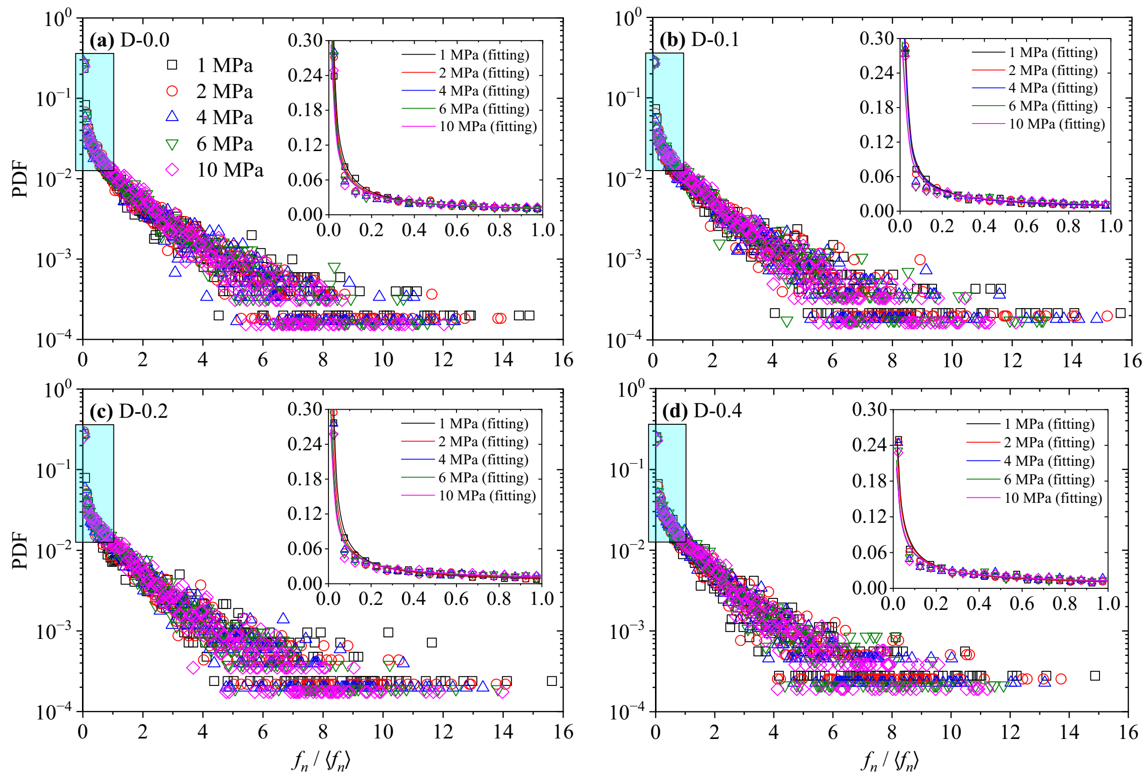

Fig. 13 Probability distribution function of normal contact forces f_n normalized by the average $\langle f_n \rangle$ in log-linear scale: **a** D-0.0; **b** D-0.1; **c** D-0.2; **d** D-0.4

decreasing magnitude, are ϕ_1, ϕ_2, ϕ_3. To quantify the fabric anisotropy, a deviatoric fabric δ_d proposed by Barreto et al. [76] is adopted as follows

$$\delta_d = \sqrt{\frac{(\phi_1 - \phi_2)^2 + (\phi_2 - \phi_3)^2 + (\phi_1 - \phi_3)^2}{2}} \tag{14}$$

Radjai et al. [77] proposed that the average normal force $\langle f_n \rangle$ is a characteristic force separating the interparticle contacts into two complementary groups: the "weak" contacts bearing forces smaller than the average and the "strong" contacts bearing forces larger than the average. Numerous numerical studies have shown that the distribution of weak contact forces is nearly isotropic, indicating that the weak forces only contribute to the isotropic stress or have little contribution to the deviatoric stress [64, 77–80]. Take specimen D-0.1 for example, the value of δ_d for strong contacts (δ_d^s) is higher than the weak contacts, indicating that the strong contacts are much more anisotropic and much more similar to that of the K_0 versus σ_v curve, as shown in Fig. 14a. Furthermore, the shape of the contact normal distribution for weak contacts is close to a sphere because the distribution of weak contacts is approximately isotropic, and the shape for strong contacts, by contrast, is thin in the middle, as shown in Fig. 14b and c.

In terms of the link between the macroscopic behavior and the strong force network, Essayah et al. [81] found that the deviatoric stress in the triaxial test is carried by strong contacts, and Mahmud Sazzad et al. [82] and Mahmud Sazzad [83] found that the tendency of δ_d for strong contacts coincides with the stress–strain curve of granular material during cyclic loading and true triaxial loading. To emphasize the main ideas and to allow for concise analytical discussion, the contribution of the strong contacts to the stress tensor is considered here only.

Figure 15 shows the evolution of δ_d^s under the effect of PSD. The δ_d^s increases initially with increasing vertical stress σ_v and then gradually levels off. The value of δ_d^s and strong contact proportion depends on the PSD. The specimen with lower C_u induces higher anisotropy and more strong contacts during compression, in which a lower value of K_0 is measured.

Figure 16 shows the evolution of δ_d^s under the effect of RR. The value of δ_d^s and strong contact proportion also depends on the RR coefficient, which has less influence than the PSD. The specimen with higher μ_r induces higher anisotropy and more strong contacts during compression, in which a lower value of K_0 is measured. These findings imply that a possible correlation exists between δ_d^s and K_0 in one-dimensional tests.

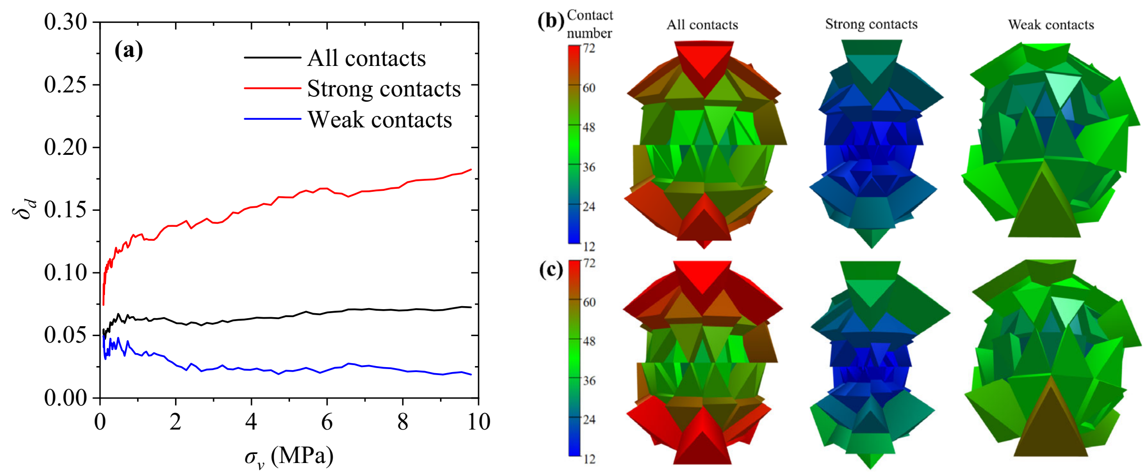

Fig. 14 Deviatoric fabric and contact normal distribution in D-0.1: **a** δ_d; **b** 4 MPa; **c** 10 MPa

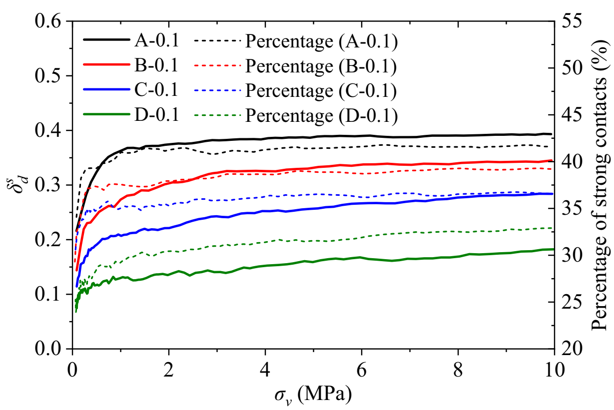

Fig. 15 Evolution and percentage of δ_d^s under the effect of PSD

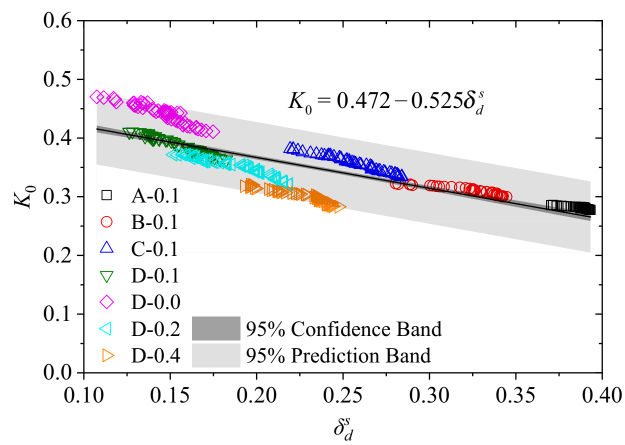

Fig. 17 Relationship between K_0 and δ_d^s for all specimens

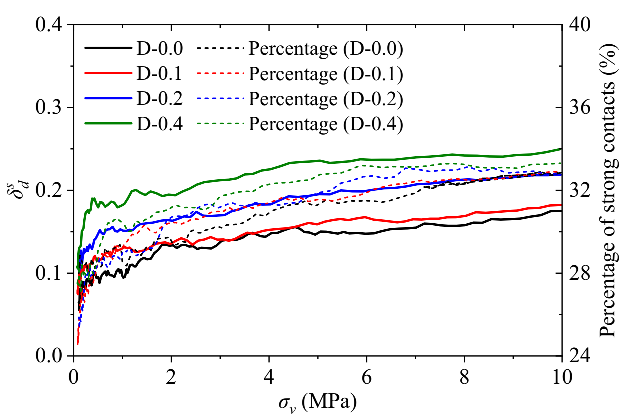

Fig. 16 Evolution and percentage of δ_d^s under the effect of RR

3.5 Relationship between K_0 and fabric anisotropy

Figure 17 shows the relationship between K_0 and fabric anisotropy of strong contacts δ_d^s. It is worth noting that a good linear relationship between K_0 and δ_d^s is established as the strong contacts are used to quantify the fabric tensors. This linear relationship demonstrates unequivocally that K_0 measured through the rigid walls on the macro-level is directly connected with the fabric anisotropy of strong contacts on the micro-level.

4 Conclusion

DEM simulations of one-dimensional compression tests were carried out to investigate the effects of PSD and RR on K_0 and the corresponding microscopic behaviors of sands. A non-spherical particle was introduced in the DEM model. A macro–micro relationship between K_0 and fabric anisotropy of strong contacts δ_d^s is established. Some interesting findings are summarized below.

(1) After the vertical stress reaches a certain value, K_0 gradually decreases and approaches a comparatively stable value as vertical stress reaches 10 MPa. K_0 of the specimen with a larger C_u runs above those with a lower C_u. This is attributed to the strong force chain along the vertical direction due to more significant interlocking, resulting in a lower degree of stress transfer in the horizontal direction.
(2) K_0 of the specimen with a lower μ_r runs above those with a higher μ_r. Similar to the above, lower K_0 from the specimen with a higher μ_r can be attributed to the strong force chain along the vertical direction due to more intense friction between particles.
(3) PSD and RR significantly affect the evolution of the coordination number. The higher C_u, the lower the mean CN is. The relative mean CN decreases linearly with increasing relative C_u regardless of the influence of vertical stress. Additionally, increasing μ_r causes a monotonic decrease in the mean CN, and too much consideration of RR makes the mean CN less realistic in a particle system.
(4) RDF of the specimen with higher C_u shows that the polydisperse specimen is more ordered than the monodisperse one. However, the effect of RR on the RDF is negligible. The PDF(f_n) maintains a nearly constant distribution regardless of the influence of vertical stress. For the specimen with monodisperse particles, the PDF(f_n) for normal contact force f_n less than the average$\langle f_n \rangle$fits well with the Gaussian distribution, while PDF(f_n) fits well with the power law as C_u increases. PDF(f_n) above$\langle f_n \rangle$for each specimen is characterized by an exponential distribution, from which the inhomogeneity of normal forces enhances as C_u increases and slightly reduces as μ_r increases.
(5) Strong contacts are much more anisotropic than weak ones. A unique macro–micro relationship exists between K_0 and deviatoric fabric when strong contacts are considered only.

Acknowledgements The authors gratefully acknowledge the support received from the National Science Foundation of the Jiangsu Higher Education Institutions of China (23KJB170022), Key Project of Natural Science Foundation of Henan Province (232300421134), and First-Class Discipline Implementation of Safety Science and Engineering (AQ20230103), China.

Data availability The datasets generated during and/or analyzed during the current study are available from the corresponding author on reasonable request.\

Declarations

Competing interest The authors declared that they have no conflicts of interest to this work.

References

1. Mesri G, Hayat TM (1993) The coefficient of earth pressure at rest. Can Geotech J 30:647–666. https://doi.org/10.1139/t93-056
2. Michalowski RL (2005) Coefficient of earth pressure at rest. J Geotech Geoenviron Eng 131:1429–1433. https://doi.org/10.2208/jscej1969.1979.284_59
3. Gao Y, Yu Z, Chen W et al (2023) Recognition of rock materials after high- temperature deterioration based on SEM images via deep learning. J Mater Res Technol 25:273–284. https://doi.org/10.1016/j.jmrt.2023.05.271
4. Lirer S, Flora A, Nicotera MV (2011) Some remarks on the coefficient of earth pressure at rest in compacted sandy gravel. Acta Geotech 6:1–12. https://doi.org/10.1007/s11440-010-0131-2
5. Talesnick M, Nachum S, Frydman S (2021) K0 determination using improved experimental technique. Geotechnique 71:509–520. https://doi.org/10.1680/jgeot.19.P.019
6. Jaky J (1944) The coefficient of earth pressure at rest. J Soc Hung Archit Eng 78:355–358. https://doi.org/10.1139/t94-090
7. Mayne PW, Kulhawy FH (1982) K0–OCR relationships in soil. J Geotech Eng Div 108:851–869
8. Lee J, Yun TS, Lee D, Lee J (2013) Assessment of K0 correlation to strength for granular materials. Soils Found 53:584–595. https://doi.org/10.1016/j.sandf.2013.06.009
9. Zhao X, Zhou G, Tian Q, Kuang L (2010) Coefficient of earth pressure at rest for normal, consolidated soils. Min Sci Technol 20:406–410. https://doi.org/10.1016/S1674-5264(09)60216-7
10. Monroy R, Zdravkovic L, Ridley AM (2015) Mechanical behaviour of unsaturated expansive clay under K0 conditions. Eng Geol 197:112–131. https://doi.org/10.1016/j.enggeo.2015.08.006
11. Abbas MF, Elkady TY, Al-Shamrani MA (2015) Evaluation of strain and stress states of a compacted highly expansive soil using a thin-walled oedometer. Eng Geol 193:132–145. https://doi.org/10.1016/j.enggeo.2015.04.012
12. Kim J, Seol Y, Dai S (2021) The coefficient of earth pressure at rest in hydrate-bearing sediments. Acta Geotech 16:2729–2739. https://doi.org/10.1007/s11440-021-01174-0
13. Northcutt S, Wijewickreme D (2013) Effect of particle fabric on the coefficient of lateral earth pressure observed during one-dimensional compression of sand. Can Geotech J 50:457–466. https://doi.org/10.1139/cgj-2012-0162
14. Tong C, Burton GJ, Zhang S, Sheng D (2020) Particle breakage of uniformly graded carbonate sands in dry/wet condition subjected to compression/shear tests. Acta Geotech 15:2379–2394. https://doi.org/10.1007/s11440-020-00931-x
15. Zhu JG, Jiang MJ, Lu YY et al (2018) Experimental study on the K0 coefficient of sandy gravel under different loading conditions. Granul Matter 20:40. https://doi.org/10.1007/s10035-018-0814-1
16. Chu J, Gan CL (2004) Effect of void ratio on K0 of loose sand. Geotechnique 54:285–288. https://doi.org/10.1680/geot.2004.54.4.285
17. Teerachaikulpanich N, Okumura S, Matsunaga K, Ohta H (2007) Estimation of coefficient of earth pressure at rest using modified oedometer test. Soils Found 47:349–360. https://doi.org/10.3208/sandf.47.349
18. Guo P (2010) Effect of density and compressibility on K0 of cohesionless soils. Acta Geotech 5:225–238. https://doi.org/10.1007/s11440-010-0125-0
19. Okochi Y, Tatsuoka F (1984) Some factors affecting K0-values of sand measured in triaxial cell. Soils Found 24:52–68
20. Hatanaka M, Uchida A, Taya Y (1999) Estimation of K0-value of in-situ gravelly soils. Soils Found 39:93–101. https://doi.org/10.3208/sandf.39.5
21. Fioravante V, Jamiolkowski M, Lo Presti DCF et al (1998) Assessment of the coefficient of the earth pressure at rest from shear wave

velocity measurements. Geotechnique 48:657–666. https://doi.org/10.1680/geot.1998.48.5.657
22. Tong L, Liu L, Cai G, Du G (2013) Assessing the coefficient of the earth pressure at rest from shear wave velocity and electrical resistivity measurements. Eng Geol 163:122–131. https://doi.org/10.1016/j.enggeo.2013.05.012
23. Pegah E, Liu H (2020) Evaluating the overconsolidation ratios and peak friction angles of granular soil deposits using noninvasive seismic surveying. Acta Geotech 15:3193–3209. https://doi.org/10.1007/s11440-020-00953-5
24. Cundall PA, Strack ODL (1979) A discrete numerical model for granular assemblies. Geotechnique 29:47–65. https://doi.org/10.1680/geot.1980.30.3.331
25. Gu X, Hu J, Huang M (2015) K0 of granular soils: a particulate approach. Granul Matter 17:703–715. https://doi.org/10.1007/s10035-015-0588-7
26. Gu X, Hu J, Huang M, Yang J (2018) Discrete element analysis of the K 0 of granular soil and its relation to small strain shear stiffness. Int J Geomech 18:06018003. https://doi.org/10.1061/(asce)gm.1943-5622.0001102
27. Lopera Perez JC, Kwok CY, O'Sullivan C et al (2015) Numerical study of one-dimensional compression in granular materials. Geotech Lett 5:96–103. https://doi.org/10.1680/jgele.14.00107
28. Khalili MH, Roux JN, Pereira JM et al (2017) A numerical study of one-dimensional compression of granular materials: I. Stress-strain behavior, microstructure, and irreversibility. Phys Rev E. https://doi.org/10.1103/PhysRevE.95.032907
29. Chen H, Zhao S, Zhao J, Zhou X (2021) The microscopic origin of K0 on granular soils: the role of particle shape. Acta Geotech 16:2089–2109. https://doi.org/10.1007/s11440-021-01161-5
30. Shi J, Haegeman W, Andries J (2021) Investigation on the mechanical properties of a calcareous sand: the role of the initial fabric. Mar Georesources Geotechnol 39:859–875. https://doi.org/10.1080/1064119X.2020.1775327
31. Wu Y, Yamamoto H, Izumi A (2016) Experimental investigation on crushing of granular material in one-dimensional test. Period Polytech Civ Eng 60:27–36. https://doi.org/10.3311/PPci.8028
32. Zhao J, Zhao S, Luding S (2023) The role of particle shape in computational modelling of granular matter. Nat Rev Phys 5:505–525. https://doi.org/10.1038/s42254-023-00617-9
33. Guo PJ, Stolle DFE (2006) Fabric and particle shape influence on K0 of granular materials. Soils Found 46:639–652
34. Han S, Wang C, Liu X et al (2023) A random algorithm for 3D modeling of solid particles considering elongation, flatness, sphericity, and convexity. Comput Part Mech 10:19–44. https://doi.org/10.1007/s40571-022-00475-9
35. Valera RLR, González JI, de Oliveira JM et al (2023) Development and coupling of numerical techniques for modeling micromechanical discrete and continuous media using real particle morphologies. Comput Part Mech 10:121–141. https://doi.org/10.1007/s40571-022-00481-x
36. Zhang T, Zhang C, Zou J et al (2020) DEM exploration of the effect of particle shape on particle breakage in granular assemblies. Comput Geotech 122:103542. https://doi.org/10.1016/j.compgeo.2020.103542
37. Zhang T, Yang W, Zhang C, Hu C (2021) Particle breakage effect on compression behavior of realistic granular assembly. Int J Geomech 21:1–12. https://doi.org/10.1061/(asce)gm.1943-5622.0002022
38. Zhang T, Zhang C, Song F et al (2023) Breakage behavior of silica sands during high-pressure triaxial loading using X-ray microtomography. Acta Geotech. https://doi.org/10.1007/s11440-023-01866-9
39. Chen H, Zhao S, Zhou X (2020) DEM investigation of angle of repose for super-ellipsoidal particles. Particuology 50:53–66. https://doi.org/10.1016/j.partic.2019.05.005
40. Fang C, Gong J, Jia M et al (2021) DEM simulation of the shear behaviour of breakable granular materials with various angularities. Adv Powder Technol 32:4058–4069. https://doi.org/10.1016/j.apt.2021.09.009
41. Nie JY, Zhao J, Cui YF, Li DQ (2022) Correlation between grain shape and critical state characteristics of uniformly graded sands: a 3D DEM study. Acta Geotech 17:2783–2798. https://doi.org/10.1007/s11440-021-01362-y
42. Tian J, Liu E (2019) Influences of particle shape on evolutions of force-chain and micro-macro parameters at critical state for granular materials. Powder Technol 354:906–921. https://doi.org/10.1016/j.powtec.2019.07.018
43. Wu M, Wu F, Wang J (2022) Particle shape effect on the shear banding in DEM-simulated sands. Granul Matter 24:48. https://doi.org/10.1007/s10035-022-01210-0
44. Jia Y, Xu B, Chi S et al (2019) Particle breakage of rockfill material during triaxial tests under complex stress paths. Int J Geomech 19:04019124. https://doi.org/10.1061/(asce)gm.1943-5622.0001517
45. Yang H, Zhou B, Wang J (2019) Exploring the effect of 3D grain shape on the packing and mechanical behaviour of sands. Geotech Lett 9:299–304. https://doi.org/10.1680/jgele.18.00227
46. Zhang T, Zhang C, Yang Q, Fu R (2020) Inter-particle friction and particle sphericity effects on isotropic compression behavior in real-shaped sand assemblies. Comput Geotech 126:103741. https://doi.org/10.1016/j.compgeo.2020.103741
47. Aela P, Zong L, Yin ZY et al (2023) Calibration method for discrete element modeling of ballast particles. Comput Part Mech 10:481–493. https://doi.org/10.1007/s40571-022-00507-4
48. Bandeira AA, Zohdi TI (2019) 3D numerical simulations of granular materials using DEM models considering rolling phenomena. Comput Part Mech 6:97–131. https://doi.org/10.1007/s40571-018-0200-0
49. Estrada N, Azeóma E, Radjai F, Taboada A (2013) Comparison of the effects of rolling resistance and angularity in sheared granular media. In: AIP conference proceedings, vol 1542. pp 891–894. https://doi.org/10.1063/1.4812075
50. Fukumoto Y, Sakaguchi H, Murakami A (2013) The role of rolling friction in granular packing. Granul Matter 15:175–182. https://doi.org/10.1007/s10035-013-0398-8
51. Santos AP, Bolintineanu DS, Grest GS et al (2020) Granular packings with sliding, rolling, and twisting friction. Phys Rev E 102:32903. https://doi.org/10.1103/PhysRevE.102.032903
52. Zhao S, Evans TM, Zhou X (2018) Shear-induced anisotropy of granular materials with rolling resistance and particle shape effects. Int J Solids Struct 150:268–281. https://doi.org/10.1016/j.ijsolstr.2018.06.024
53. Iwashita K, Oda M (1998) Rolling resistance at contacts in simulation of shear band. J Eng Mech 124:285–292
54. Jiang MJ, Yu HS, Harris D (2005) A novel discrete model for granular material incorporating rolling resistance. Comput Geotech 32:340–357. https://doi.org/10.1016/j.compgeo.2005.05.001
55. Ai J, Chen JF, Rotter JM, Ooi JY (2011) Assessment of rolling resistance models in discrete element simulations. Powder Technol 206:269–282. https://doi.org/10.1016/j.powtec.2010.09.030
56. Wensrich CM, Katterfeld A (2012) Rolling friction as a technique for modelling particle shape in DEM. Powder Technol 217:409–417. https://doi.org/10.1016/j.powtec.2011.10.057
57. Presti DCFL, Pallara O, Froio F et al (2006) Stress-strain-strength behaviour of undisturbed and reconstituted gravelly soil samples. Riv Ital di Geotec 40:9–27
58. Wadell H (1932) Volume, shape, and roundness particles. J Geol 40:443–451
59. Thornton C, Antony SJ (1998) Quasi-static deformation of particulate media. Philos Trans R Soc A Math Phys Eng Sci 356:2763–2782. https://doi.org/10.1098/rsta.1998.0296

60. Makse HA, Johnson DL, Schwartz LM (2000) Packing of compressible granular materials. Phys Rev Lett 84:4160–4163. https://doi.org/10.1103/PhysRevLett.84.4160
61. Zhao B, Wang J, Andò E et al (2020) Investigation of particle breakage under one-dimensional compression of sand using x-ray microtomography. Can Geotech J 57:754–762. https://doi.org/10.1139/cgj-2018-0548
62. Al-Raoush R (2007) Microstructure characterization of granular materials. Phys A Stat Mech its Appl 377:545–558. https://doi.org/10.1016/j.physa.2006.11.090
63. Conzelmann NA, Penn A, Partl MN et al (2020) Link between packing morphology and the distribution of contact forces and stresses in packings of highly nonconvex particles. Phys Rev E 102:1–13. https://doi.org/10.1103/PhysRevE.102.062902
64. Joseph Antony S (2001) Evolution of force distribution in three-dimensional granular media. Phys Rev E 63:011302. https://doi.org/10.1103/PhysRevE.63.011302
65. Silbert LE, Ertaş D, Grest GS et al (2002) Geometry of frictionless and frictional sphere packings. Phys Rev E 65:031304. https://doi.org/10.1103/PhysRevE.65.031304
66. Aste T (2005) Variations around disordered close packing. J Phys Condens Matter 17:S2361. https://doi.org/10.1088/0953-8984/17/24/001
67. Zhao S, Zhao J, Guo N (2020) Universality of internal structure characteristics in granular media under shear. Phys Rev E 101:12906. https://doi.org/10.1103/PhysRevE.101.012906
68. Kramar M, Goullet A, Kondic L, Mischaikow K (2013) Persistence of force networks in compressed granular media. Phys Rev E 87:042207. https://doi.org/10.1103/PhysRevE.87.042207
69. Ma G, Zhou W, Chang X-L, Yuan W (2014) Combined FEM/DEM Modeling of triaxial compression tests for rockfills with polyhedral particles. Int J Geomech 14:04014014. https://doi.org/10.1061/(asce)gm.1943-5622.0000372
70. Liu J, Wu X, Jiang J et al (2023) A network-based investigation on the strong contact system of granular materials under isotropic and deviatoric stress states. Comput Geotech 153:105077. https://doi.org/10.1016/j.compgeo.2022.105077
71. Estrada N, Oquendo WF (2017) Microstructure as a function of the grain size distribution for packings of frictionless disks: Effects of the size span and the shape of the distribution. Phys Rev E 96:1–8. https://doi.org/10.1103/PhysRevE.96.042907
72. An N, Ma G, Zhou H et al (2023) DEM investigation of the microscopic mechanism of scale effect of sandy gravel material. Acta Geotech 18:1373–1390. https://doi.org/10.1007/s11440-022-01667-6
73. Cantor D, Azéma E, Azéma E, Preechawuttipong I (2020) Microstructural analysis of sheared polydisperse polyhedral grains. Phys Rev E 101:62901. https://doi.org/10.1103/PhysRevE.101.062901
74. Mutabaruka P, Taiebat M, Pellenq RJM, Radjai F (2019) Effects of size polydispersity on random close-packed configurations of spherical particles. Phys Rev E 100:42906. https://doi.org/10.1103/PhysRevE.100.042906
75. Satake M (1992) A discrete-mechanical approach to granular materials. Int J Eng Sci 30:1525–1533. https://doi.org/10.1016/0020-7225(92)90162-A
76. Barreto D, O'Sullivan C, Zdravkovic L (2009) Quantifying the evolution of soil fabric under different stress paths. In: AIP conference proceedings, vol 1145. pp 181–184. https://doi.org/10.1063/1.3179881
77. Radjai F, Wolf DE, Jean M, Moreau JJ (1998) Bimodal character of stress transmission in granular packings. Phys Rev Lett 80:61–64. https://doi.org/10.1103/PhysRevLett.80.61
78. Minh NH, Cheng YP, Thornton C (2014) Strong force networks in granular mixtures. Granul Matter 16:69–78. https://doi.org/10.1007/s10035-013-0455-3
79. Huang X, Hanley KJ, O'Sullivan C, Kwok CY (2014) Exploring the influence of interparticle friction on critical state behaviour using DEM. Int J Numer Anal Methods Geomech 38:1276–1297. https://doi.org/10.1002/nag.2259
80. Azéma E, Radjaï F (2012) Force chains and contact network topology in sheared packings of elongated particles. Phys Rev E 85:031303. https://doi.org/10.1103/PhysRevE.85.031303
81. Essayah A, Shire T, Gao Z (2022) The relationship between contact network and energy dissipation in granular materials. Granul Matter 24:100. https://doi.org/10.1007/s10035-022-01255-1
82. Mahmud Sazzad M, Suzuki K, Modaressi-Farahmand-Razavi A (2012) Macro-micro responses of granular materials under different b values using DEM. Int J Geomech 12:220–228. https://doi.org/10.1061/(asce)gm.1943-5622.0000133
83. Mahmud Sazzad M (2014) Micro-scale behavior of granular materials during cyclic loading. Particuology 16:132–141. https://doi.org/10.1016/j.partic.2013.12.005